



# Monoclinic dibismuth tetraoxide: A new visible-light-driven photocatalyst for environmental remediation

Wanjun Wang<sup>a</sup>, Xingqiu Chen<sup>b</sup>, Gang Liu<sup>b</sup>, Zhurui Shen<sup>a,c</sup>, Dehua Xia<sup>d</sup>, Po Keung Wong<sup>d</sup>, Jimmy C. Yu<sup>a,\*</sup>

<sup>a</sup> Department of Chemistry and Institute of Environment, Energy and Sustainability, The Chinese University of Hong Kong, Shatin, N.T., Hong Kong, China

<sup>b</sup> Shenyang National Laboratory for Materials Science, Institute of Metal Research, Chinese Academy of Sciences, 72 Wenhua Road, Shenyang 110016, China

<sup>c</sup> Key Laboratory of Advanced Ceramics and Machining Technology, Ministry of Education, School of Materials Science and Engineering, Tianjin University, Tianjin 300072, China

<sup>d</sup> School of Life Sciences, The Chinese University of Hong Kong, Shatin, N.T., Hong Kong, China

## ARTICLE INFO

### Article history:

Received 5 February 2015

Received in revised form 8 April 2015

Accepted 15 April 2015

Available online 17 April 2015

### Keywords:

Photocatalysis

Bismuth oxide

Pollutant degradation

Bacterial disinfection

## ABSTRACT

A new visible-light-driven photocatalyst, monoclinic dibismuth tetraoxide ( $m\text{-Bi}_2\text{O}_4$ ), has been discovered. This simple oxide with mixed valent states ( $\text{Bi}^{3+}$  and  $\text{Bi}^{5+}$ ) has a band gap energy of 2.0 eV, and is responsive to wavelength up to 620 nm. The first-principle calculations within the hybrid density functional framework (HSE) indicate that  $m\text{-Bi}_2\text{O}_4$  is a typical indirect-gap semiconductor. It shows much higher photocatalytic degradation activity as well as photostability than some of the well-investigated highly efficient photocatalysts, such as  $\text{CdS}$  and  $\text{Bi}_2\text{O}_3$ . Not only typical dyes and colorless aromatic compounds, including rhodamine B, methyl orange, methyl blue, phenol and 4-nitrophenol, but also bacterial (*Escherichia coli*) cells can be effectively degraded/inactivated in the presence of  $m\text{-Bi}_2\text{O}_4$ . The electronic potential of band structure is studied and a photocatalytic mechanism is also proposed, in which both  $\cdot\text{OH}$  and direct  $h^+$  oxidation play important roles in the degradation process. Our discovery highlights the potential of developing  $\text{Bi}_2\text{O}_4$ -based photocatalysts as a new class of highly active, stable and safe photocatalyst for versatile pollutant degradation and disinfection under visible light.

© 2015 Published by Elsevier B.V.

## 1. Introduction

The degradation of organic pollutants and the inactivation of pathogenic bacteria in wastewater are two of the most important issues for environmental remediation. Photocatalysis has attracted broad interest because it allows for the direct use of abundant sunlight or artificial light to drive a powerful oxidation process for breaking down various bioresistant organic contaminants, including dyes and bacteria [1]. However, the most widely used  $\text{TiO}_2$  photocatalyst is only active under UV irradiation which accounts for only 4% of the sunlight spectrum. Therefore, one of the central missions for the success of environmental photocatalysis is to find a more effective photocatalytic system that can work under sunlight. In particular, the search of visible-light-driven photocatalysts has been an intensively pursued topic during the past few decades,

because a large portion (43%) of solar energy locates in the visible light region [2].

Over the last few decades, the development of visible-light-driven photocatalysts has evolved from modified  $\text{TiO}_2$  [3,4] to non- $\text{TiO}_2$  based semiconductor materials, mainly including metal oxides, sulfides, oxynitrides or oxysulfides (e.g.,  $\text{TiO}_{2-x}\text{N}_x$ ,  $\text{TaON}$ ,  $\text{LaTiO}_2\text{N}$ ,  $\text{GaN:ZnO}$ ,  $\text{Sm}_2\text{Ti}_2\text{O}_5\text{S}_2$ ), and some transition metal complexes (e.g., ruthenium(II)-tris-bipyridine, iron hydrogenase enzymes) [5]. Bismuth-based photocatalysts such as  $\text{Bi}_2\text{O}_3$  [6,7],  $\text{BiO}_{1.84}\text{H}_{0.08}$  [8],  $\text{BiVO}_4$  [9,10],  $\text{Bi}_2\text{WO}_6$  [11],  $\text{Bi}_2\text{MoO}_6$  [12],  $\text{BiOX}$  ( $X = \text{Cl}, \text{Br}, \text{I}$ ) [13],  $\text{Bi}_5\text{O}_7\text{I}$  [14] and  $\text{PbBi}_2\text{Nb}_2\text{O}_9$  [15], are particularly useful because they are environmentally benign and have high photo-stability. Among these compounds, the simple binary oxides are much more promising for practical application, because they have unique advantages of simple structure, low costs, facile synthesis and easy to scale up for commercial applications.

It is known that bismuth exists in trivalent or pentavalent states in oxides. The hybridized  $\text{O}2p$  and  $\text{Bi}6s^2$  valence bands in  $\text{Bi}^{3+}$ -containing oxides leads to the narrow band gap and visible-light-responsive activity, while the empty  $6s$  orbital of  $\text{Bi}^{5+}$  also

\* Corresponding author. Tel.: +852 3943 6268; fax: +852 2603 5057.  
E-mail address: [jimmy@cuhk.edu.hk](mailto:jimmy@cuhk.edu.hk) (J.C. Yu).

supports the high visible light photocatalytic activity for  $\text{Bi}^{5+}$ -containing compounds [16]. However, simple bismuth oxides with mixed valent states have rarely been reported. Begemann and Janson [17] prepared a cubic  $\text{Bi}_2\text{O}_{4-x}$  for the first time by thermal decomposition of  $\text{HBiO}_3 \cdot n\text{H}_2\text{O}$  and amorphous  $\text{Bi}_2\text{O}_5$  under high oxygen pressures, but the crystal structure details of this oxide were not given. Prakash et al. [18] further synthesized the cubic  $\text{Bi}_2\text{O}_{4-x}$  by oxidative precipitation using  $\text{Na}_2\text{S}_2\text{O}_8$  as the oxidant, and suggested the cubic fluorite related structures are stabilized by some amount of  $\text{Bi}^{5+}$ , which upon thermal treatment is reduced to  $\text{Bi}^{3+}$  with release of  $\text{O}_2$  to finally transform to  $\text{Bi}_2\text{O}_3$ . In 1995, Kumada et al. [19,20] found another mixed valent bismuth oxide of monoclinic dibismuth tetraoxide (m- $\text{Bi}_2\text{O}_4$ ) with  $\beta\text{-Sb}_2\text{O}_4$ -type structure. Thermal properties were investigated but no application was suggested for the product. Recently, Hameed et al. reported a photon induced formation of  $\text{Bi}_2\text{O}_{4-x}$  at the surface of  $\text{Bi}_2\text{O}_3$  for enhanced photocatalytic activity toward the mineralization of 2-chloro and 2-nitrophenol [21]. The formation of minor concentration of  $\text{Bi}_2\text{O}_{4-x}$  entities enhances the visible light harvesting and photocatalytic activity. This result indicates the m- $\text{Bi}_2\text{O}_4$  may be another narrow band semiconductor for photocatalytic applications under visible light.

Herein, we systematically investigated the crystal structure, optical property, band structure and electronic structure of m- $\text{Bi}_2\text{O}_4$ , and found that the m- $\text{Bi}_2\text{O}_4$  could be a new and stable visible-light-driven photocatalyst with sufficient photocatalytic activity not only for organic pollutants degradation, but also for bacterial inactivation.

## 2. Experimental

### 2.1. Materials preparation and characterizations

The m- $\text{Bi}_2\text{O}_4$  used in this study was synthesized through a simple hydrothermal method by using  $\text{NaBiO}_3$  as the solely starting material. Typically, 0.56 g  $\text{NaBiO}_3$  (International Laboratory, USA, 99%) powder was dispersed in water and put into a 20 mL Teflon-lined stainless autoclave. The autoclave was sealed and heated in an oven at  $160^\circ\text{C}$  for 5–12 h under autogenous pressure. The resulting product was collected by centrifugation at 6000 rpm, washed with deionized water and dried at  $55^\circ\text{C}$  overnight.

X-ray diffraction (XRD) patterns were recorded with a Rigaku SmartLab X-ray diffractometer using  $\text{Cu K}\alpha 1$  irradiation ( $\lambda = 1.5406 \text{ \AA}$ ). The accelerating voltage and applied current were 40 kV and 40 mA, respectively. UV–vis diffuse reflectance spectrum (UV–vis DRS) was obtained for the dry-pressed disk sample using a Varian Cary 500 UV–vis spectrophotometer equipped with a labSphere diffuse reflectance accessory.  $\text{BaSO}_4$  was used as a reflectance standard in the UV–vis DRS experiment. The morphology of the product was characterized by scanning electron microscopy (FESEM, FEI, Quanta 400 FEG) and transmission electron microscopy (TEM, FEI Tecnai G2 Spirit). HRTEM was obtained on a FEI Tecnai F20 transmission electron microscopy operated at 200 kV. The surface electronic states were analyzed by X-ray photoelectron spectroscopy (XPS, PerkinElmer PHI 5000). All the binding energy values were calibrated by using  $\text{C}1\text{s} = 284.6 \text{ eV}$  as a reference. Total organic carbon (TOC) analysis was conducted by auto-sampler ASI-V connecting to the TOC analyzer TOC-V<sub>CSH/CSN</sub> (Shimadzu Corporation, Kyoto, Japan). The generation of  $\bullet\text{OH}$  was investigated through the method of photoluminescence with terephthalic acid. The  $\bullet\text{OH}$  was captured by terephthalic acid to produce a fluorescent product 2-hydroxyterephthalic acid [22] and then analyzed by a fluorescence spectrophotometer (Hitachi F-4500, excitation wavelength: 320 nm; fluorescence peak: 425 nm). The surface area was measured by the Brunauer–Emmett–Teller

(BET) method using nitrogen adsorption–desorption isotherms at 77 K with a Micromeritics ASAP 2020 instrument. Metal ion release was tested by inductively coupled plasma optical emission spectrometer (ICP-OES, PerkinElmer Optima 4300 DV). Thermogravimetric analysis (TGA) was performed in  $\text{N}_2$  flow (20 mL/min) using a thermogravimetric analyzer (Netzsch STA 449C). The samples were heated from room temperature to  $700^\circ\text{C}$  at a rate of  $10^\circ\text{C}/\text{min}$ . The amount of  $\text{Bi(V)}$  was determined by iodometry using 0.1 M  $\text{Na}_2\text{S}_2\text{O}_3$  as the titrant, and 1% starch solution as the indicator [18,19].

### 2.2. Mott–Schottky plot

The Mott–Schottky plots were obtained from electrochemical impedance measurements, which were carried out on an electrochemical workstation (CHI 660D, Shanghai Chen Hua Instrument Company, China). The working electrode was prepared on indium-tin oxide (ITO) glasses, which was cleaned by sonication in chloroform, acetone and ethanol for 30 min, respectively. The glass was then rinsed with water and kept in isopropanol for 24 h. Five-milligrams of the as-prepared m- $\text{Bi}_2\text{O}_4$  and 10  $\mu\text{L}$  of Nafion solution (5 wt%) were dispersed in a 1 mL water/isopropanol mixed solvent (3:1 v/v) by sonication to form a homogeneous catalyst colloid. Then, 100  $\mu\text{L}$  of the catalyst colloid was deposited onto the ITO glass with areas of about  $1 \text{ cm}^2$ . Electrochemical impedance measurements were performed in a conventional three electrode cell, using a Pt plate and a saturated  $\text{Ag/AgCl}$  electrode as counter electrode and reference electrode, respectively. The working electrodes were immersed in a 0.05 M  $\text{Na}_2\text{SO}_4$  aqueous solution without additive for 30 s before measurement was carried out. The potential ranged from  $-1.0$  to  $0.5 \text{ V}$  (vs.  $\text{Ag/AgCl}$ ) with the frequency settled at 1.5 or 1.0 kHz.

### 2.3. Theoretical calculation details

We performed DFT calculations using the Vienna ab initio Simulation Package (VASP) code with the projector-augmented wave (PAW) scheme [23]. The different approximations have been used to treat the xc energy. The semilocal GGA of Perdew, Burke, and Ernzerhof (PBE) [24] and the hybrid xc developed by Heyd, Scuseria and Ernzerhof (HSE) which was already supplemented in VASP [25,26]. In particular, the hybrid functional mixes exact exchange in the Hartree–Fock (HF) from with a semilocal PBE xc function:

$$E_{xc}^{\text{HSE}} = \alpha E_{xc}^{\text{HF},\text{sr}}(\mu) + (1 - \alpha) E_{xc}^{\text{PBE},\text{sr}} + \alpha E_{xc}^{\text{PBE},\text{lr}} + E_{xc}^{\text{PBE}} \quad (1)$$

where  $\mu = 0.20 \text{ \AA}^{-1}$  controls the range separation between the short-range (sr) and long-range (lr) part of the Coulomb kernel, and the parameter  $\alpha$  determines the fraction of exact HF exchange incorporated. Here, we adopted the standard choice of  $\alpha = 0.25$  for HSE calculations. We used a Fermi smearing of electronic occupancy with a width of 0.05 eV, and a plane-wave cutoff energy of 500 eV, which has been found to be sufficient for precise energetics for all the elements considered in present work. The structural relaxations including ionic positions were full optimized according the energetic and stress minimizations. The quasi-Newton algorithm was used to capture the minimum energy. The optimized lattice parameters of m- $\text{Bi}_2\text{O}_4$  were further compiled in the Supplementary material (see Table S1), evidencing a nice agreement with the experimentally measured data [20].

### 2.4. Photocatalytic activity measurements

The photocatalytic activity for organic pollutants degradation was initially evaluated by measuring the photodegradation of Rhodamine B (RhB) under visible light. In a typical measurement, 30 mg

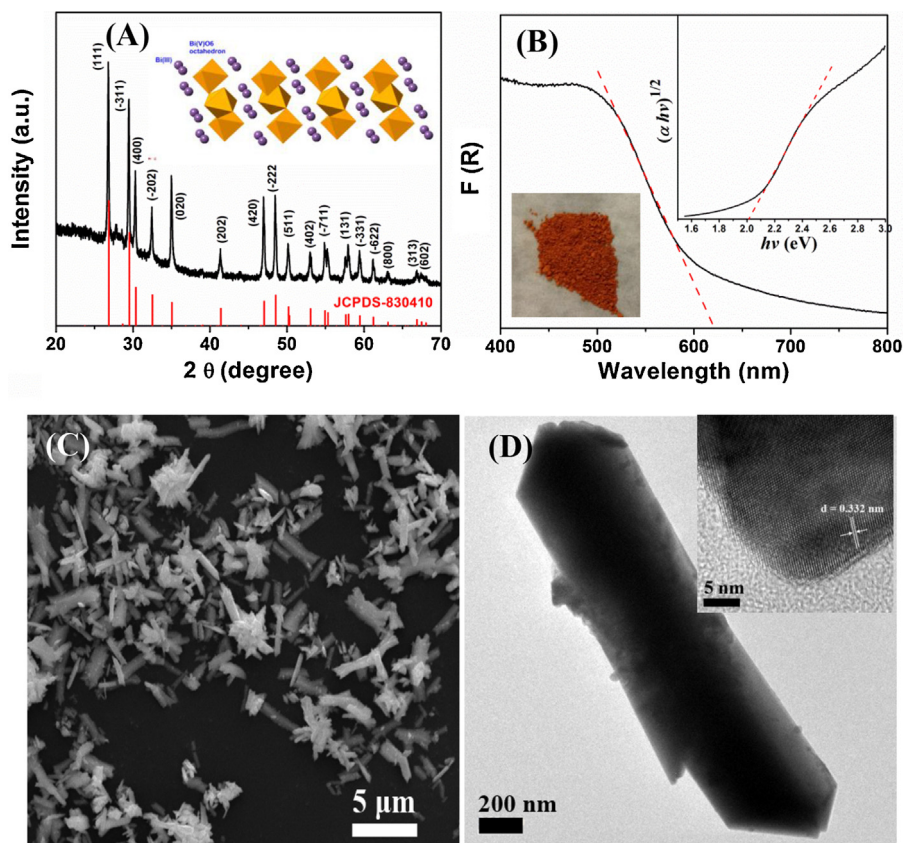


**Fig. 1.** (A) X-ray diffraction (XRD) pattern of the m-Bi<sub>2</sub>O<sub>4</sub> (Inset: crystal structure of m-Bi<sub>2</sub>O<sub>4</sub>); (B) UV-vis diffuse reflectance spectrum (UV-vis DRS) of m-Bi<sub>2</sub>O<sub>4</sub>; (C) Scanning electron microscopy (SEM) image, and (D) Transmission electron microscopy (TEM) image of m-Bi<sub>2</sub>O<sub>4</sub> (Inset: HRTEM of m-Bi<sub>2</sub>O<sub>4</sub>).

photocatalysts were suspended in 20 mL of 10 ppm aqueous solution of RhB. The solution was stirred in dark for 20 min to achieve the equilibrium adsorption. Then the suspension was illuminated with a 300 W xenon lamp with a cutoff filter ( $\lambda > 400$  nm), and the average light intensity was about 960 mW/cm<sup>2</sup>. The concentration change of RhB was monitored by measuring the UV-vis absorption of the supernatants after removing the photocatalysts by centrifugation. The peak absorbance of RhB at 554 nm was used to determine its concentration. As a comparison, commercially available CdS (Farco Chemical Supplies, 99%) and  $\beta$ -Bi<sub>2</sub>O<sub>3</sub> (Aladdin, 99.9%) were used as reference photocatalysts. Several other organic pollutants, including methylene blue (MB, 10 ppm), methyl orange (MO, 20 ppm), phenol (20 ppm) and 4-nitrophenol (4-NP, 20 ppm) were also used to test the universality of the photocatalytic organic pollutants degradation by m-Bi<sub>2</sub>O<sub>4</sub>. The detection wavelength were 664, 464, 269 and 400 nm (after adjusting the pH to 9) [27], for MB, MO, phenol and 4-NP, respectively.

The photocatalytic activity for bacterial inactivation was conducted by disinfection of *Escherichia coli* K-12 cells. The final photocatalyst concentration and cell density were adjusted to 100 mg/L and  $2 \times 10^7$  cfu (colony forming unit)/mL, respectively. The detailed experimental procedures for bacterial incubation, sampling and detection can be found in our previous reports [10,28]. For bacterial fluorescence spectroscopy, the cells were fluorescently stained with the dyes of LIVE/DEAD BacLight bacterial viability kit (L7012, Molecular Probes, Inc., Eugene, OR) according to procedures recommended by the manufacturer. After being incubated at 25 °C in the dark for 15 min, the samples were examined using a fluorescence microscopy (Nikon ECLIPSE 80i, Japan) equipped with a filter block N UV-2A consisting of excitation filter Ex 330–380 (Nikon, Japan) and Spot-K slider CCD camera (Diagnostic instruments. Inc., USA).

### 3. Results and discussion

#### 3.1. Characterization of m-Bi<sub>2</sub>O<sub>4</sub>

The m-Bi<sub>2</sub>O<sub>4</sub> used in this study was synthesized through a simple hydrothermal method by using NaBiO<sub>3</sub> as the solely starting material without adding any additives. Fig. 1A shows the XRD of the m-Bi<sub>2</sub>O<sub>4</sub> prepared at 160 °C for 12 h. It is clear that all the diffraction can be well indexed to the monoclinic phase of Bi<sub>2</sub>O<sub>4</sub> (JCPDS-830410). It can be regarded as a mixed valent bismuth oxide with the formula of Bi<sup>3+</sup>Bi<sup>5+</sup>O<sub>4</sub>. In this crystal structure, the Bi<sup>5+</sup>O<sub>6</sub> octahedra form layers parallel to (1 0 0) by sharing four corners with each other. The Bi<sup>3+</sup> ions are located in the interlayer position (inset of Fig. 1A) [20]. The influence of hydrothermal reaction time was studied, and the results showed that the NaBiO<sub>3</sub> began to decompose to produce m-Bi<sub>2</sub>O<sub>4</sub> after 1 h, while pure phase could be obtained after 5 h (Fig. S1). The crystallinity of the products increase with extended reaction time, and we therefore use the sample prepared at 12 h for further characterizations throughout the study.

The optical absorption of m-Bi<sub>2</sub>O<sub>4</sub> was measured by diffuse reflectance spectroscopy (Fig. 1B). The absorption cutoff wavelength determined by the steep absorption locates at about 620 nm, suggesting that the present material may be visible-light-responsive. As can be expected from the absorption spectra, the m-Bi<sub>2</sub>O<sub>4</sub> is reddish orange in color (inset of Fig. 1B). The energy band gap ( $E_g$ ) of semiconductor can be estimated by using the expression  $\alpha h\nu = A(h\nu - E_g)^n$  [29,30], where  $\alpha$  is the absorption coefficient,  $h\nu$  is the photon energy, and  $n = 2$  for m-Bi<sub>2</sub>O<sub>4</sub> as a indirect transition semiconductor (See theoretical calculation results). The  $E_g$  is measured with the help of absorption spectra and a graph of  $(\alpha h\nu)^{1/2}$  versus  $h\nu$  is plotted (inset of Fig. 1B). The extrapolation



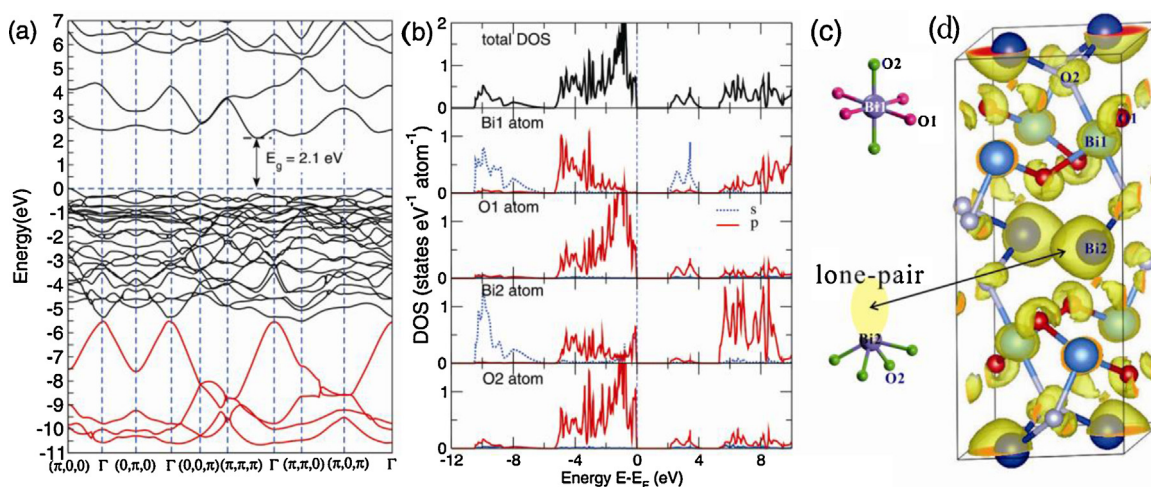


**Fig. 2.** Electronic structures of m-Bi<sub>2</sub>O<sub>4</sub>. (a) Electronic band structure, (b) total and partial densities of states, (c) local coordination of both Bi1 at the 4c site and Bi2 at the 4e site, (d) the isosurface with an ELF isovalue of 0.8 of the derived electron localization function (ELF).

of the straight line to  $(\alpha h\nu)^{1/2} = 0$  gives the value of  $E_g$  to be about 2.0 eV.

The SEM image of the as-prepared m-Bi<sub>2</sub>O<sub>4</sub> shows a submicrorods morphology (Fig. 1C). Typical HRTEM image confirms the m-Bi<sub>2</sub>O<sub>4</sub> submicrorods has a diameter of about 500 nm and a length of about 4–5  $\mu\text{m}$ . The clear lattice fringes of  $d = 0.332$  nm match those of the (1 1 1) lattice plane of m-Bi<sub>2</sub>O<sub>4</sub> (Fig. 1D). High resolution XPS spectrum further confirms the mixed valence state of bismuth in this oxide. The Bi 4f<sub>7/2</sub> (or 4f<sub>5/2</sub>) peak can be deconvoluted well into two bimodal peaks at binding energy of 158.4 and 159.1 eV (or at 163.7 and 164.4 eV), which are attributed to Bi(III) and Bi(V), respectively (see Fig. 4C). The mixed valence state of bismuth was also characterized by TGA and iodometry. As shown in Fig. 4D, the first weight loss from 260 °C to 300 °C is due to partial reduction of Bi(V) to Bi(III) with the formation of “Bi<sub>4</sub>O<sub>7</sub>” (=Bi<sub>2</sub>O<sub>3.5</sub>) [18,19], while the second weight loss is due to complete reduction of Bi(V) with the formation of Bi<sub>2</sub>O<sub>3</sub>. The total weight loss (3.3 wt%) was in agreement with the calculated value on the assumption that m-Bi<sub>2</sub>O<sub>4</sub> changes to Bi<sub>2</sub>O<sub>3</sub> by release of oxygen, which indicates the Bi(V) and Bi(III) content is approximately equal in m-Bi<sub>2</sub>O<sub>4</sub>. In addition, the Bi(V) content determined by iodometry was 43.7 wt%, which agrees well with the calculated value (43.4%) in Bi<sup>3+</sup>Bi<sup>5+</sup>O<sub>4</sub>.

### 3.2. Theoretical calculation

To understand the electronic structure of m-Bi<sub>2</sub>O<sub>4</sub>, we further performed the first-principle calculations within the hybrid density functional framework (HSE), which has been proven to be a more accurate one [26] for semiconductor than the conventional density functional theory. The derived results were further compiled in Fig. 2. The HSE calculation demonstrates that m-Bi<sub>2</sub>O<sub>4</sub> is a typical indirect-gap semiconductor with the minimum band gap of 2.1 eV (see Fig. 2a). This derived size of the band gap is in perfect agreement with the experimentally measured data (2.0 eV). In particular, from the derived densities of states (DOSs) as shown in Fig. 2b, several clear features have been observed. The occupied electronic states consist of two major groups. The lowest-energy states in the energy range from –11 eV to –5.5 eV below the top of the valence band mostly consist of Bi s-like states, as illustrated in Fig. 2b for both Bi1 and Bi2 atom at the 4c and 4e sites, respectively. The second group of the occupied states, ranging from –5.5 eV to the top of the valence band, consisting of typical ionic bonding features between Bi1 (or Bi2) p-like and O1 (O2)

p-like states. Importantly, note that the top of the valence band mainly stems from the electronic hybridized states between Bi2 atom and O2 atom, but dominated by the O2 p-like state as illustrated in Fig. 2c. Interestingly, the unoccupied electronic states are also characteristic of two different groups (Fig. 2b). In the first, in the energetic range from 2.1 eV to 4 eV the electronic states come from the antibonding state of the electronic hybridization between Bi1 s-like and O1 (and O2) p-like states occurring in each BiO<sub>6</sub> octahedron (Fig. 2c). In the second, in the higher energy range from 5.7 eV to 10 eV the electronic states obviously originate from the unoccupied antibonding states of the ionic bonding electronic states between Bi1 (and Bi2) p-like and O1 (and O2) p-like states. This second unoccupied group certainly corresponds to both the local environments for both Bi1 and Bi2 atoms (Fig. 2c). From the above analysis, it can be noted that m-Bi<sub>2</sub>O<sub>4</sub> is indeed a charge-transfer semiconductor with the O2 p-like dominated top of the valence band and the Bi1 s-like bottom of the conduction bands.

From the viewpoint of the chemical bonding, m-Bi<sub>2</sub>O<sub>4</sub> exhibits a highly unique feature. As illustrated in Fig. 2b, although both Bi1 and Bi2 atoms have the common lowest-energy electronic states mostly comprised from their s-like states in the energy range from –11 eV to –5.5 eV, the mechanism of their appearances is intrinsically different. For the Bi1 atom, these states indeed occur due to the strong electronic hybridizations between Bi s-like and O1 (and O2) p-like states. This type of electronic hybridization induces these lowest-energy bonding states from –11 eV to –5.5 eV and the unoccupied antibonding states in the energy range from 2.1 eV to 4 eV. This is the reason as to why m-Bi<sub>2</sub>O<sub>4</sub> has two isolated unoccupied bands just above the 2.1 eV band gap. However, the different behavior has been observed for the Bi2 atoms. Its lowest-energy s-like states also in the energy range from –11 eV to –5.5 eV are the nonbonding states, which relate to a long-paired s orbital of each Bi2 atom (Fig. 2c). Its nonbonding nature is illustrated by the isosurface of the derived electron localization function (ELF) in Fig. 2d, which clearly localized at the space adjacent to the Bi2 atom. The different behaviors of the Bi1 and Bi2 atoms interpret well the mixed valent states of the Bi atoms in m-Bi<sub>2</sub>O<sub>4</sub>. Because the electrons of both s- and p-like orbitals participate in the ionic bonding with their neighboring O1 and O2 atoms in the BiO<sub>6</sub> octahedral framework, the Bi atom has a Bi<sup>5+</sup> (V) electronic configuration, whereas, because of the existence of the fully occupied s lone-pair orbital, the Bi2 atom only has the Bi<sup>3+</sup> (III) configuration by transferring its three electrons at the p-like orbitals to its neighboring O2 atom.

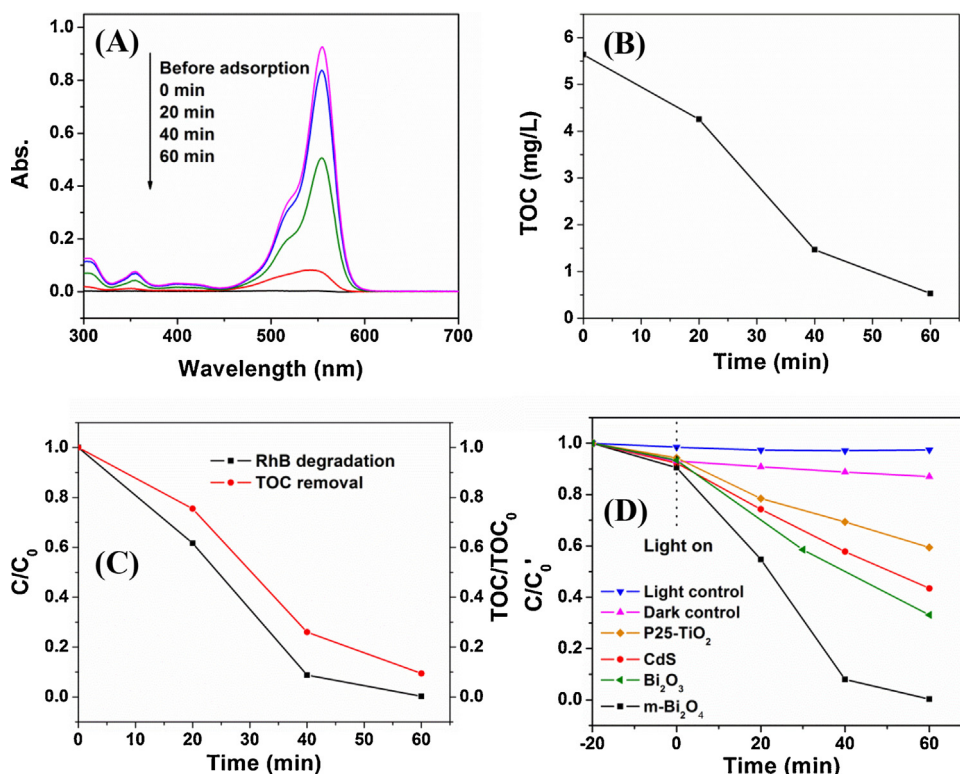


**Fig. 3.** (A) UV-vis spectral changes of RhB (10 ppm, 20 mL) in m-Bi<sub>2</sub>O<sub>4</sub> (30 mg) suspensions under visible light irradiation; (B) Changes in TOC during the photocatalytic degradation of RhB; (C) Simultaneously monitoring the concentration and TOC changes of RhB during the photocatalytic degradation process by m-Bi<sub>2</sub>O<sub>4</sub>; (D) Concentration changes of RhB at 554 nm as a function of irradiation time in the presence of Bi<sub>2</sub>O<sub>3</sub>, CdS, P25-TiO<sub>2</sub> and m-Bi<sub>2</sub>O<sub>4</sub> ( $C_0$ : concentration before absorption).

### 3.3. Photocatalytic degradation of RhB

The photocatalytic activity of m-Bi<sub>2</sub>O<sub>4</sub> was initially evaluated by degradation of aqueous RhB as a model probe under visible light ( $\lambda > 400$  nm) illumination. The control experiments demonstrated that RhB dye is stable in aqueous solution under visible light irradiation in the absence of a photocatalyst, while m-Bi<sub>2</sub>O<sub>4</sub> alone has no degradation ability toward RhB under dark condition. With light on, the RhB undergoes fast decolorization in the presence of m-Bi<sub>2</sub>O<sub>4</sub>, and complete decolorization can be achieved within 60 min (Fig. 3A). The TOC change was monitored during the decolorization process (Fig. 3B and C). It shows that the mineralization process of RhB is consistent with the decolorization process, and the mineralization yield reaches a value of 90.6% after 60 min of visible light irradiation. These results indicate that the RhB is photocatalytically degraded rather than decolorized in the presence m-Bi<sub>2</sub>O<sub>4</sub>.

Two commercially available visible-light-driven photocatalysts, CdS and  $\beta$ -Bi<sub>2</sub>O<sub>3</sub>, were used to compare their photocatalytic activity with m-Bi<sub>2</sub>O<sub>4</sub>. CdS is one of the most active visible-light-driven photocatalysts but it severely suffers from photocorrosion [31,32].  $\beta$ -Bi<sub>2</sub>O<sub>3</sub> is another simple binary oxide in Bi-based photocatalytic family, and is reported to have the highest photocatalytic oxidation activity toward organic pollutants degradation among the other three crystal phase structure (i.e.,  $\alpha$ -,  $\gamma$ -,  $\delta$ -Bi<sub>2</sub>O<sub>3</sub>) [33,34]. As shown in Fig. 3D, m-Bi<sub>2</sub>O<sub>4</sub> is much more active than CdS and  $\beta$ -Bi<sub>2</sub>O<sub>3</sub>. The BET surface area is measured to be 3.65, 3.59 and 23.63 m<sup>2</sup> g<sup>-1</sup> for m-Bi<sub>2</sub>O<sub>4</sub>,  $\beta$ -Bi<sub>2</sub>O<sub>3</sub> and CdS, respectively. It shows that the surface area of m-Bi<sub>2</sub>O<sub>4</sub> and  $\beta$ -Bi<sub>2</sub>O<sub>3</sub> is similar, which is even lower than that of CdS. Therefore, the highest activity of m-Bi<sub>2</sub>O<sub>4</sub> is not due to external factors (e.g., surface area). To quantify the degradation rates, we applied the pseudo-first-order model which is widely used to study the kinetics in photocatalytic degradation reactions. The obtained apparent rate constant  $k$  is 0.0228, 0.0088 and 0.0109 min<sup>-1</sup> for

m-Bi<sub>2</sub>O<sub>4</sub>, CdS and  $\beta$ -Bi<sub>2</sub>O<sub>3</sub>, respectively. This result indicates that the photocatalytic degradation activity of m-Bi<sub>2</sub>O<sub>4</sub> is 2.6 and 2.1 times higher than CdS and  $\beta$ -Bi<sub>2</sub>O<sub>3</sub>, respectively. In addition, the Degussa P25-TiO<sub>2</sub> was also used as a standard photocatalyst for comparison. Since TiO<sub>2</sub> is not active under visible light irradiation, it shows much lower activity than that of CdS, Bi<sub>2</sub>O<sub>3</sub> and m-Bi<sub>2</sub>O<sub>4</sub>. The observed moderate decolorization of RhB by P25-TiO<sub>2</sub> may be mainly due to photosensitization.

Photostability is a key consideration in choosing a photocatalyst. We measured the leaching of metal ion release by ICP-OES during the RhB degradation process with extended visible light irradiation for 5 h (Fig. S2). It shows that a very high Cd<sup>2+</sup> release (712 ppm) was found in the case of CdS, while no detectable metal ions from m-Bi<sub>2</sub>O<sub>4</sub>, indicating that the m-Bi<sub>2</sub>O<sub>4</sub> is quite stable and would not cause any secondary pollution. The recyclability was also tested for four runs (Fig. 4A). Results show that the photocatalytic activity remains the same for the first three runs, and only decreases a little (6%) in the fourth run, which may due to the slightly inactivation of the catalyst caused by surface adsorption of small molecular fragments during degradation. The structural stability of this photocatalyst was further examined by XRD analysis before and after photocatalytic degradation (Fig. 4B). No obvious change in XRD pattern was found, indicating its good crystal stability. Furthermore, High resolution XPS analysis was also conducted to carefully study the Bi surface states (Fig. 4C). It shows that the surface Bi(V) to Bi(III) ratio decreased a little after the reaction. This can be rationalized by considering the fierce photocatalytic redox reactions occurring on the catalyst surface, resulting in the partial reduction of Bi(V) to Bi(III) on the surface. Although m-Bi<sub>2</sub>O<sub>4</sub> is considered to be a metastable phase of Bi oxides [20], our results indicate that it is stable under photocatalytic redox reactions and only some surface Bi(V) could be reduced to Bi(III) which would in turn protect bulk Bi(V) from further reduction. The TGA curve



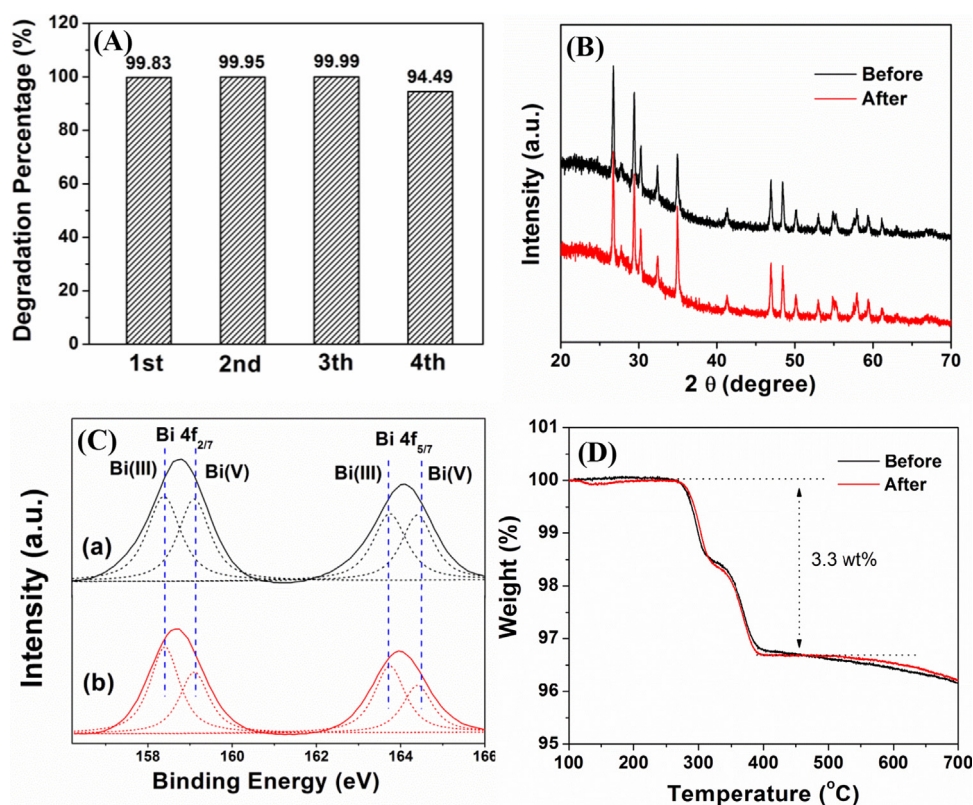


**Fig. 4.** (A) Cycling runs in the photocatalytic degradation of RhB in the presence of m-Bi<sub>2</sub>O<sub>4</sub>; (B) XRD pattern of m-Bi<sub>2</sub>O<sub>4</sub> before and after photocatalytic degradation process showing no obvious differences; (C) High resolution X-ray photoemission (XPS) spectra of Bi 4f orbits before (a) and after (b) photocatalytic degradation; (D) Thermogravimetric analysis (TGA) of m-Bi<sub>2</sub>O<sub>4</sub> before and after photocatalytic degradation process.

profile and the total weight loss remain almost the same before and after photocatalytic reaction (Fig. 4D), suggesting the minimum loss of bulk Bi(V) in the m-Bi<sub>2</sub>O<sub>4</sub>.

### 3.4. Photocatalytic degradation of phenol and other pollutants

To further confirm the activity of m-Bi<sub>2</sub>O<sub>4</sub>, colorless phenol degradation was conducted under visible light, as the RhB may undergo photosensitization mechanisms [35]. As shown in Fig. 5, CdS and P25-TiO<sub>2</sub> shows negligible activity toward phenol degradation, while about 45% of phenol is degraded in the presence of β-Bi<sub>2</sub>O<sub>3</sub>. Interestingly, about 90% of phenol is removed within 120 min in the case of m-Bi<sub>2</sub>O<sub>4</sub>, and complete degradation is achieved within 180 min. No degradation is found in the dark,

indicating the phenol is photocatalytically degraded by m-Bi<sub>2</sub>O<sub>4</sub>. It should be noted that phenols are very hard to be degraded due to resonance stability [36]. It is a pleasant surprise that m-Bi<sub>2</sub>O<sub>4</sub> can do it so efficiently under visible light.

Beside phenol, several other typical dyes and colorless aromatic compounds were also tested, including methyl orange (MO), methyl blue (MB) and 4-nitrophenol. No dark reaction occurs in the presence of m-Bi<sub>2</sub>O<sub>4</sub>. With visible light irradiation, more than 90% of MO and MB can be decolorized within 40 min, while about 85% 4-nitrophenol are degraded within 120 min, respectively (Fig. 6). It is found that the degradation of colorless compounds is much slower than that of dyes, which may be attributed to the synthetic effect of photosensitization and photocatalytic oxidation in the case of dye degradation. Nevertheless, this novel simple oxide photocatalyst is

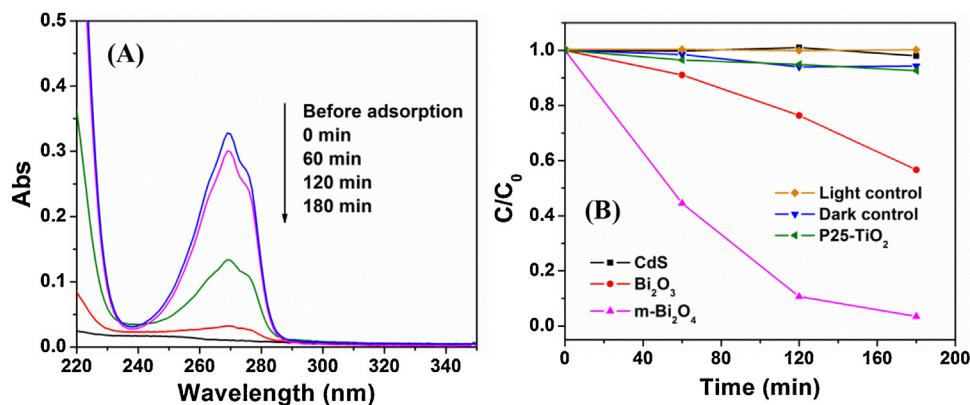


**Fig. 5.** (A) UV-vis spectral changes of phenol (20 ppm, 20 mL) in m-Bi<sub>2</sub>O<sub>4</sub> (30 mg) suspensions under visible light irradiation; (B) Concentration changes of phenol at 269 nm as a function of irradiation time in the presence of Bi<sub>2</sub>O<sub>3</sub>, CdS, P25-TiO<sub>2</sub> and m-Bi<sub>2</sub>O<sub>4</sub> (C<sub>0</sub>: concentration after adsorption).

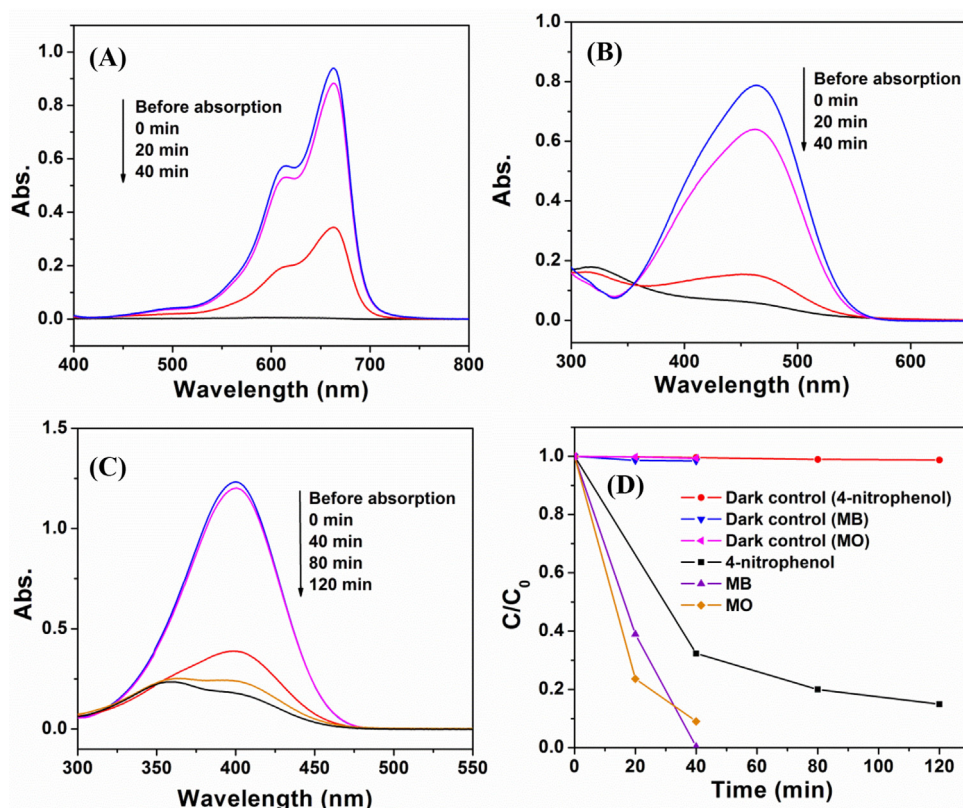


**Fig. 6.** (A) UV-vis spectral changes of MB (10 ppm, 20 mL), (B) MO (20 ppm, 20 mL), and (C) 4-nitrophenol (20 ppm, 20 mL) in the presence of m-Bi<sub>2</sub>O<sub>4</sub> (30 mg) under visible light irradiation; (D) Concentration changes of MB, MO and 4-nitrophenol as a function of irradiation time in the presence of m-Bi<sub>2</sub>O<sub>4</sub> (C<sub>0</sub>: concentration after absorption).

expected to exhibit universal photo-degradation activity toward organic pollutants without obvious selectivity.

### 3.5. Photocatalytic bacterial disinfection

To examine its possibility to be used in photocatalytic water disinfection, *E. coli* K-12 was chosen as a representative microorganism to evaluate the photocatalytic inactivation performances of m-Bi<sub>2</sub>O<sub>4</sub>. In the dark and light control experiments, the bacterial population remained unchanged, indicating no toxic effect of m-Bi<sub>2</sub>O<sub>4</sub> to *E. coli* K-12 cells and no photolysis of bacterial cells under visible light irradiation alone. With visible light irradiation, the m-Bi<sub>2</sub>O<sub>4</sub> exhibited remarkable photocatalytic activity for the inactivation of *E. coli* K-12, and total inactivation of about 7 log of bacterial cells was achieved after 120 min of irradiation in the presence of 100 mg/L m-Bi<sub>2</sub>O<sub>4</sub> (Fig. 7). This bacterial inactivation activity is much higher than most of our previously reported photocatalysts for disinfection, including B-Ni-TiO<sub>2</sub> [37], BiVO<sub>4</sub> [10], CdIn<sub>2</sub>S<sub>4</sub> [30], natural sphalerite [38] and g-C<sub>3</sub>N<sub>4</sub>/graphene co-wrapped  $\alpha$ -S<sub>8</sub> [28] under identical experimental conditions, except for some Ag-containing photocatalysts (i.e., Ag/AgBr/Bi<sub>2</sub>WO<sub>6</sub>) [39] which are highly efficient but inherently toxic to the environment because of the potential toxicity of Ag<sup>0</sup>/Ag<sup>+</sup> species [40].

To further confirm the photocatalytic bactericidal effect of m-Bi<sub>2</sub>O<sub>4</sub>, the BacLight kit fluorescent microscopic method was conducted [39,41]. The cells were stained with the mixtures of SYTO 9 green-fluorescent nucleic acid stain and red-fluorescent nucleic acid stain, propidium iodide, which are typical cell-labeling dyes, respectively for the detection of living and dead bacterial cells. Fig. 8A shows that the living cells before photocatalytic treatment exhibits intense green fluorescence. After visible light irradiation

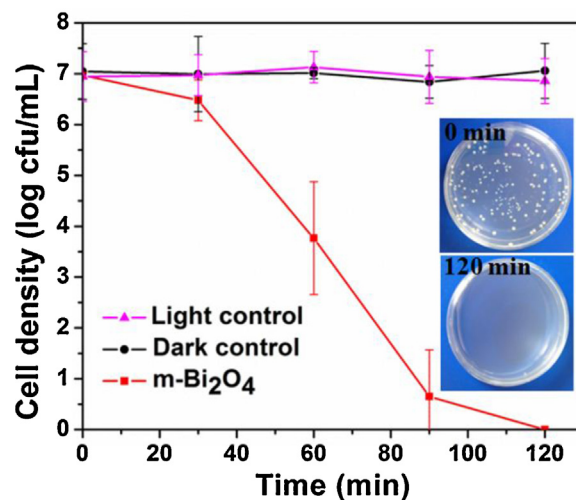


**Fig. 7.** Photocatalytic inactivation efficiency against *E. coli* K-12 ( $2 \times 10^7$  cfu/mL, 50 mL) in the presence of m-Bi<sub>2</sub>O<sub>4</sub> (5 mg) under visible light irradiation.

for 30 min, some bacterial cells exhibited red fluorescence, indicating partial amounts of the cells were inactivated during the visible light photocatalytic process (Fig. 8B). With prolonged irradiation time, few and no living bacteria were observed after 60 and 120 min, respectively (Fig. 8C and D). Moreover, to determine the possible bacterial regrowth, the reaction mixture after photocatalytic treatment for 120 min was sampled and underwent a 96 h recovery period. No detectable bacterial count (in cfu/mL) was observed after 96 h dark incubation period, indicating the photocatalytic inactivation by m-Bi<sub>2</sub>O<sub>4</sub> leads to irreversible damage to *E. coli* K-12 cells.



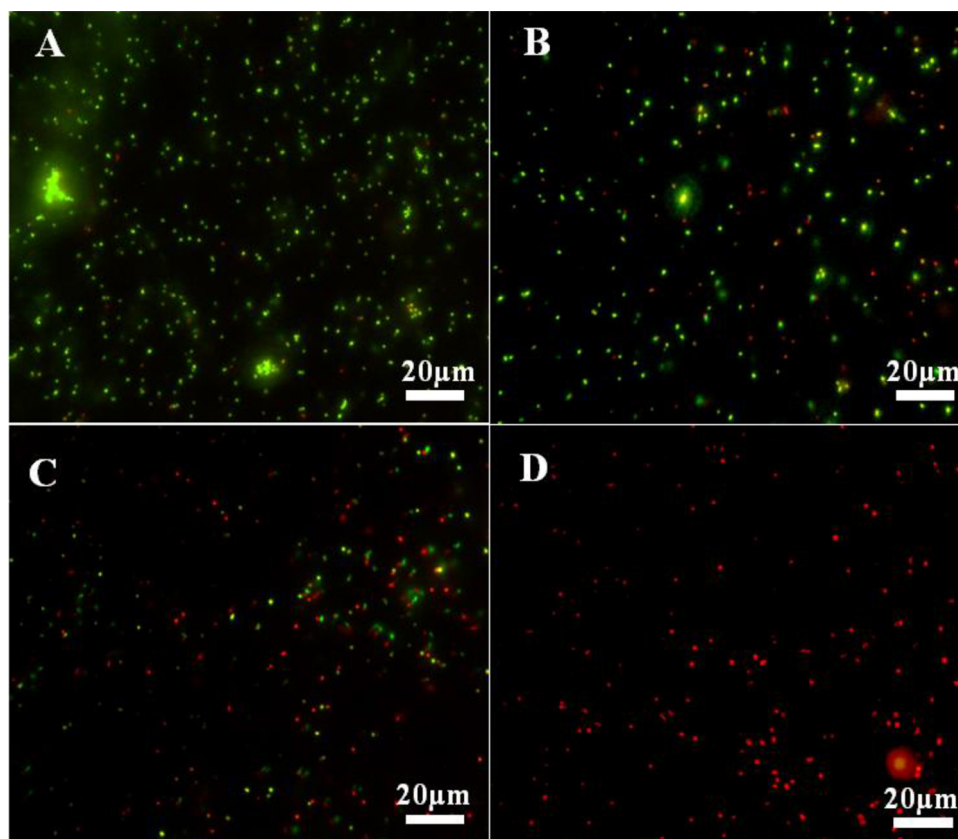


**Fig. 8.** Fluorescence microscopic images of *E. Coli* K-12 ( $2 \times 10^7$  cfu/mL, 50 mL) photocatalytically treated by m-Bi<sub>2</sub>O<sub>4</sub> (5 mg) under visible light irradiation for (A) 0, (B) 30, (C) 60, and (D) 120 min.

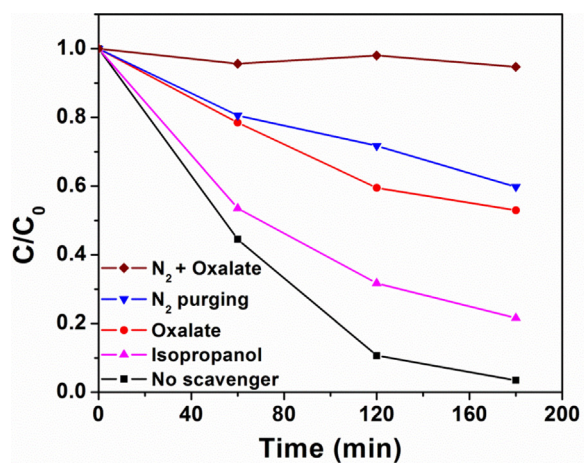


**Fig. 9.** Concentration changes of phenol (20 ppm, 20 mL) at 269 nm as a function of irradiation time in the presence of m-Bi<sub>2</sub>O<sub>4</sub> (30 mg) with 5 mM isopropanol, sodium oxalate or N<sub>2</sub> purging.

### 3.6. Photocatalytic mechanisms

The scavengers study was conducted to understand the photocatalytic oxidation process by m-Bi<sub>2</sub>O<sub>4</sub> (Fig. 9). Phenol was selected as the photocatalytic probe, as no photosensitization mechanism should occur for phenol degradation. Isopropanol was used as a scavenger of  $\bullet\text{OH}$ , because the rate constant of reaction between  $\bullet\text{OH}$  and isopropanol reaches  $1.9 \times 10^9 \text{ M}^{-1} \text{ s}^{-1}$  [42], with a rate of almost the diffusion limit. It is found that the addition of isopropanol can suppress the phenol degradation, indicating  $\bullet\text{OH}$  plays a role in the photocatalytic oxidation process. Meanwhile,

the addition of sodium oxalate as a hole scavenger also significantly suppresses the degradation efficiency, which suggests the photo-generated  $\text{h}^+$  also plays a major role. With N<sub>2</sub> purging to remove O<sub>2</sub>, the degradation efficiency decreases significantly. This may be due to the lack of  $\text{e}^-$  acceptor (i.e., O<sub>2</sub>) in the conduction band, thus increasing the undesirable photo-generated  $\text{e}^-$ - $\text{h}^+$  recombination. Note that there is still some degradation in the absence of O<sub>2</sub>, which may be attributed to the function of  $\text{h}^+$  and  $\text{h}^+$  derived radicals. When adding sodium oxalate in the case of N<sub>2</sub> purging, the degradation almost completely inhibited. These results demonstrate that both  $\bullet\text{OH}$  and  $\text{h}^+$  are responsible for the photocatalytic oxidation process.

To understand the underline intrinsic mechanism, it is crucial to locate the positions of the conduction-band minimum (CBM) and the valence-band maximum (VBM) of m-Bi<sub>2</sub>O<sub>4</sub>. For n-type semiconductors electrode, it is shown that the donor density follows the Mott–Schottky equation (Eq. (2)) [43]:

$$\frac{1}{C^2} = \left( \frac{2}{eN_d\epsilon_0\epsilon} \right) |V - V_{fb}| \quad (2)$$

where  $N_d$  is the donor density ( $\text{cm}^{-3}$ ),  $e$  is the electronic charge unit,  $\epsilon_0$  is the permittivity of the vacuum,  $\epsilon$  is the dielectric constant,  $V$  is the applied potential (V), and  $V_{fb}$  is the flat-band potential (V). It shows that when  $1/C^2$  is zero, the applied potential is equal to the flat band potential  $V_{fb}$ . Therefore, the  $V_{fb}$  can be obtained by studying the Mott–Schottky plot of m-Bi<sub>2</sub>O<sub>4</sub> films – that is,  $1/C^2$  as a function of electrochemical potentials, where the capacitance  $C$  was obtained from the impedance measurement. As shown in Fig. 10A, the positive slope of Mott–Schottky plot indicates that m-Bi<sub>2</sub>O<sub>4</sub> is an n-type semiconductor. The  $V_{fb}$  is determined to be about  $-0.5 \text{ V}$  vs. Ag/AgCl at pH 7 (equivalent to  $-0.27 \text{ V}$  vs. NHE at pH 7) [44]. It is known that the CBM in many n-type semiconductors is more



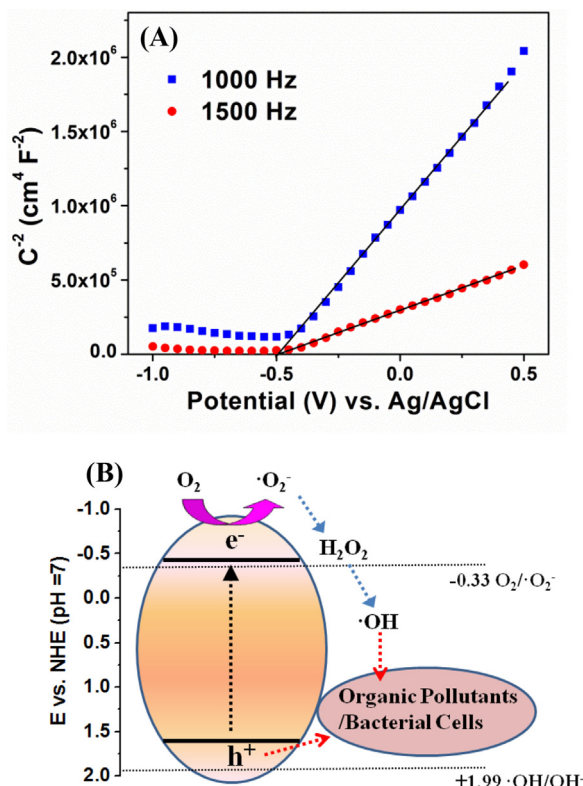
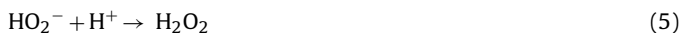
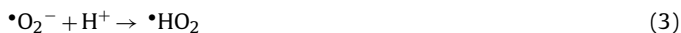


**Fig. 10.** (A) Mott-Schottky plots for m-Bi<sub>2</sub>O<sub>4</sub> according to impedance measurements. The flat-band potentials are obtained from the intercepts of the extrapolated lines. (B) Band positions of m-Bi<sub>2</sub>O<sub>4</sub> and proposed photocatalytic mechanisms.

negative by approximately,  $-0.1$  V than the  $V_{fb}$  [45]. Therefore, it is suggested that the CBM of m-Bi<sub>2</sub>O<sub>4</sub> is about  $-0.37$  V vs. NHE at pH 7. Given that the band gap energy is  $2.0$  eV, the VBM of m-Bi<sub>2</sub>O<sub>4</sub> is determined to be  $+1.63$  V vs. NHE at pH 7.

Thus, the electronic potential of CBM and VBM can be determined as illustrated in Fig. 10B. It is reported that the redox potentials for  $\bullet\text{OH}/\text{OH}^-$  and  $\text{O}_2/\bullet\text{O}_2^-$  are located at  $+1.9$  and  $-0.33$  V, respectively [46,47]. Therefore, on the conduction band, the photo-excited  $e^-$  can be trapped by  $\text{O}_2$  to produce  $\bullet\text{O}_2^-$ , which then transforms to  $\bullet\text{HO}_2$  (Eq. (3)). The  $\bullet\text{HO}_2$  is then reduced to  $\text{HO}_2^-$  and produce  $\text{H}_2\text{O}_2$  (Eqs. (4–5)). Finally,  $\bullet\text{OH}$  is generated from  $\text{H}_2\text{O}_2$  (Eq. (6)) [48]:



The generation of  $\bullet\text{OH}$  was confirmed through the method of photoluminescence with terephthalic acid (Fig. 11). It is known that  $\bullet\text{OH}$  reacts with terephthalic acid in basic solution to generate 2-hydroxyterephthalic acid, which emits a unique fluorescence signal with its peak centered at  $425$  nm. As shown in Fig. 11, significant fluorescent signals associated with 2-hydroxyterephthalic acid were generated upon visible-light irradiation of the m-Bi<sub>2</sub>O<sub>4</sub> suspended in a terephthalic acid solution for different irradiation times. In addition, the amount of  $\bullet\text{OH}$  radicals increased almost linearly with the irradiation time (Inset of Fig. 11), suggesting the stability of the photocatalytic activity.

It is noted that the energy of photo-generated  $h^+$  is not high enough to react with surface water or  $\text{OH}^-$  to produce  $\bullet\text{OH}$  at the valence band. In this case, a direct  $h^+$  oxidation process is suggested for the photocatalytic oxidation on the valence band, which

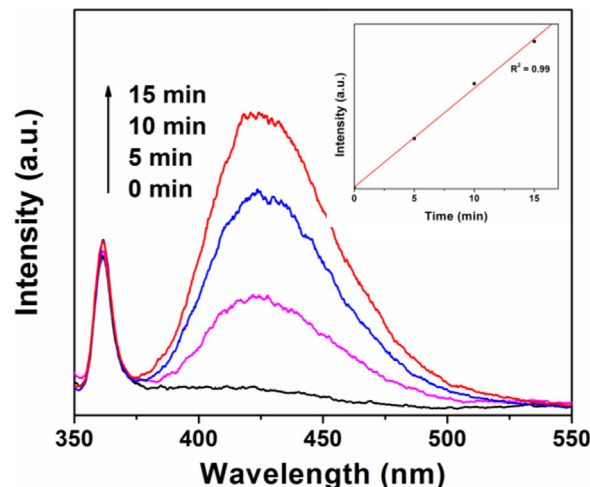


**Fig. 11.** Fluorescence emission spectral changes observed during the irradiation of m-Bi<sub>2</sub>O<sub>4</sub> with visible light irradiation in a  $4 \times 10^{-4}$  mol/L terephthalic acid and  $2 \times 10^{-3}$  mol/L NaOH (excitation at  $320$  nm).

is also evidenced by the above  $h^+$  scavenging study. For traditional photocatalytic systems, such as TiO<sub>2</sub> and CdS, the  $h^+$  will be trapped by surface  $\text{H}_2\text{O}/\text{OH}^-$  to produce  $\bullet\text{OH}$ , and the  $\bullet\text{OH}$  radicals are believed to be highly reactive and are responsible for the photocatalytic oxidation process. However, for many Bi-based photocatalysts, such as Bi<sub>2</sub>WO<sub>6</sub> [49], BiVO<sub>4</sub> [50], and BiOCl [51], reports show that  $\bullet\text{OH}$  is not detected and the photocatalytic oxidation activity is mainly attributed to the direct  $h^+$  oxidation. Notably, in the case of m-Bi<sub>2</sub>O<sub>4</sub>, both  $\bullet\text{OH}$  and direct  $h^+$  oxidation prevails in the photocatalytic process, which makes m-Bi<sub>2</sub>O<sub>4</sub> a high-efficient photocatalyst. This unique feature of band structure in m-Bi<sub>2</sub>O<sub>4</sub> may also provide useful information for the exploration of novel materials for efficient photocatalytic oxidation process.

#### 4. Conclusions

In summary, we prepared a new simple oxide (m-Bi<sub>2</sub>O<sub>4</sub>) as a highly active visible-light-driven photocatalyst for environmental remediation, including various organic pollutants degradation and bacterial disinfection. Because of a wide visible light absorption region (up to  $620$  nm) and a suitable band structure, the m-Bi<sub>2</sub>O<sub>4</sub> shows much higher activity than some of the well-investigated visible-light-driven photocatalysts (e.g., CdS, Bi<sub>2</sub>O<sub>3</sub>). The Mott-Schottky measurement indicates that it is a n-type semiconductor with the ability to produce  $\bullet\text{OH}$  through the photogenerated electrons from conduction band. As a proof-of-concept, our finds are expected to create a fertile ground for the development of next-generation visible-light-driven photocatalyst systems based on m-Bi<sub>2</sub>O<sub>4</sub>. By modification of Bi<sub>2</sub>O<sub>4</sub> through various means in the field, such as particle size and morphology control, metallic/nonmetallic doping, cocatalysts addition and heterojunctions formation with other suitable photocatalysts, a highly active, stable and safe visible-light-driven photocatalytic system may be achieved for both environmental and energy-related applications.

#### Acknowledgements

This work was partially supported by the Shenzhen Basic Research Scheme (JCY20120619151417947) and a grant from the Research Grants Council of the Hong Kong Special Administrative Region, China, under Theme-based Research Scheme through Project No. T23-407/13-N. P.K. Wong was supported by the CAS/SAFEA International Partnership Program for Creative Research Teams of Chinese Academy of Sciences, China. The authors

were grateful to Dr. Shijing Liang (Fuzhou University, China) for conducting BET surface area measurements.

## Appendix A. Supplementary data

Supplementary data associated with this article can be found, in the online version, at <http://dx.doi.org/10.1016/j.apcatb.2015.04.026>.

## References

- [1] M.R. Hoffmann, S.T. Martin, W.Y. Choi, D.W. Bahnemann, *Chem. Rev.* 95 (1995) 69–96.
- [2] C.C. Chen, W.H. Ma, J.C. Zhao, *Chem. Soc. Rev.* 39 (2010) 4206–4219.
- [3] X.X. Yang, C.D. Cao, L. Erickson, K. Hohn, R. Maghirang, K. Klabunde, *J. Catal.* 260 (2008) 128–133.
- [4] M.Y. Xing, J.L. Zhang, F. Chen, *Appl. Catal. B: Environ.* 89 (2009) 563–569.
- [5] Z.Z. Zhang, J.L. Long, L.F. Yang, W.K. Chen, W.X. Dai, X.Z. Fu, X.X. Wang, *Chem. Sci.* 2 (2011) 1826–1830.
- [6] K. Brezesinski, R. Ostermann, P. Hartmann, J. Perlich, T. Brezesinski, *Chem. Mater.* 22 (2010) 3079–3085.
- [7] Q.Z. Wang, J. Hui, L. Yang, H.H. Huang, Y.X. Cai, S.Q. Yin, Y.M. Ding, *Appl. Surf. Sci.* 289 (2014) 224–229.
- [8] P. Hu, D.F. Hou, H.Y. Shi, C.J. Chen, Y.H. Huang, X.L. Hu, *Appl. Surf. Sci.* 319 (2014) 244–249.
- [9] G.S. Li, D.Q. Zhang, J.C. Yu, *Chem. Mater.* 20 (2008) 3983–3992.
- [10] W.J. Wang, Y. Yu, T.C. An, G.Y. Li, H.Y. Yip, J.C. Yu, P.K. Wong, *Environ. Sci. Technol.* 46 (2012) 4599–4606.
- [11] C. Zhang, Y.F. Zhu, *Chem. Mater.* 17 (2005) 3537–3545.
- [12] Z.J. Zhang, W.Z. Wang, J. Ren, J.H. Xu, *Appl. Catal. B: Environ.* 123 (2012) 89–93.
- [13] J. Jiang, K. Zhao, X.Y. Xiao, L.Z. Zhang, *J. Am. Chem. Soc.* 134 (2012) 4473–4476.
- [14] J. Yang, L.J. Xu, C.L. Liu, T.P. Xie, *Appl. Surf. Sci.* 319 (2014) 265–271.
- [15] W.M. Wu, L.R. Wen, L.J. Shen, R.W. Liang, R.S. Yuan, L. Wu, *Appl. Catal. B: Environ.* 130 (2013) 163–167.
- [16] R.A. He, S.W. Cao, P. Zhou, J.G. Yu, *Chinese J. Catal.* 35 (2014) 989–1007.
- [17] B. Begemann, M. Janson, *J. Less-common Met.* 156 (1989) 123–135.
- [18] A.S. Prakash, C. Shivakumara, M.S. Hegde, L. Dupont, J.-M. Tarasco, *Mater. Res. Bull.* 42 (2007) 707–712.
- [19] N. Kinomura, N. Kumada, *Mater. Res. Bull.* 30 (1995) 129–134.
- [20] N. Kumada, N. Kinomura, P.M. Woodward, A.W. Sleight, *J. Solid State Chem.* 116 (1995) 281–285.
- [21] A. Hameed, M. Aslam, I.M.J. Ismail, N. Salah, P. Fornasiero, *Appl. Catal. B: Environ.* 163 (2015) 444–451.
- [22] C. Li, F. Wang, J. Zhu, J.C. Yu, *Appl. Catal. B: Environ.* 100 (2010) 433–439.
- [23] G. Kresse, D. Joubert, *Phys. Rev. B* 59 (1999) 1758–1775.
- [24] J.P. Perdew, K. Burke, M. Ernzerhof, *Phys. Rev. Lett.* 77 (1996) 3856–3859.
- [25] J. Heyd, G.E. Scuseria, M. Ernzerhof, *J. Chem. Phys.* 118 (2003) 8207–8223.
- [26] J. Paier, M. Marsman, G. Kresse, *J. Chem. Phys.* 127 (2007) 024103.
- [27] S.X. Li, F.Y. Zheng, W.L. Cai, A.Q. Han, Y.K. Xie, *J. Hazard. Mater.* 135 (2006) 431–436.
- [28] W.J. Wang, J.C. Yu, D.H. Xia, P.K. Wong, Y.C. Li, *Environ. Sci. Technol.* 47 (2013) 8724–8732.
- [29] K. Manickathai, S.K. Viswanathan, M. Alagar, *Indian J. Pure. Appl. Phys.* 46 (2008) 561–564.
- [30] W.J. Wang, T.W. Ng, W.K. Ho, J.H. Huang, S.J. Liang, T.C. An, G.Y. Li, J.C. Yu, P.K. Wong, *Appl. Catal. B: Environ.* 129 (2013) 482–490.
- [31] L.H. Zhang, F.Q. Sun, Y.B. Zuo, C.F. Fan, S.P. Xu, S.M. Yang, F.L. Gu, *Appl. Catal. B: Environ.* 156 (2014) 293–300.
- [32] N. Zhang, M.Q. Yang, Z.R. Tang, Y.J. Xu, *J. Catal.* 303 (2013) 60–69.
- [33] Y.H. Yan, Z.X. Zhou, Y. Cheng, L.L. Qiu, C.P. Gao, J.G. Zhou, *J. Alloys Compd.* 605 (2014) 102–108.
- [34] L.F. Yin, J.F. Niu, Z.Y. Shen, J. Chen, *Environ. Sci. Technol.* 44 (2010) 5581–5586.
- [35] J.X. Sun, G. Chen, J.Z. Wu, H.J. Dong, G.H. Xiong, *Appl. Catal. B: Environ.* 132–133 (2013) 304–314.
- [36] N.R.C.F. MacHado, V.S. Santana, *Catal. Today* 107–108 (2005) 595–601.
- [37] W.J. Wang, L.S. Zhang, T.C. An, G.Y. Li, H.Y. Yip, P.K. Wong, *Appl. Catal. B: Environ.* 108–109 (2011) 108–116.
- [38] Y.M. Chen, A.H. Lu, Y. Li, L.S. Zhang, H.Y. Yip, H.J. Zhao, T.C. An, P.K. Wong, *Environ. Sci. Technol.* 45 (2011) 5689–5695.
- [39] L.S. Zhang, K.H. Wong, H.Y. Yip, C. Hu, J.C. Yu, C.Y. Chan, P.K. Wong, *Environ. Sci. Technol.* 44 (2010) 1392–1398.
- [40] M. Bosetti, A. Masse, E. Tobin, M. Cannas, *Biomaterials* 23 (2002) 887–892.
- [41] G.Y. Li, X.L. Liu, H.M. Zhang, T.C. An, S.Q. Zhang, A.R. Carroll, H.J. Zhao, *J. Catal.* 277 (2011) 88–94.
- [42] G.V. Buxton, C.L. Greenstock, W.P. Helman, A.B. Ross, W. Tsang, *J. Phys. Chem. Ref. Data* 17 (1988) 513–886.
- [43] G. Wang, Q. Wang, W. Lu, J. Li, *J. Phys. Chem. B* 110 (2006) 22029–22034.
- [44] Q. Tian, J. Zhuang, J. Wang, L. Xie, P. Liu, *Appl. Catal. A: Gen.* 425 (2012) 74–78.
- [45] G.L. Huang, R. Shi, Y.F. Zhu, *J. Mol. Catal. A: Chem.* 348 (2011) 100–105.
- [46] M. Mrowetz, W. Balcerski, A.J. Colussi, M.R. Hoffmann, *J. Phys. Chem. B* 108 (2004) 17269–17273.
- [47] D.W. Bahnemann, M. Hilgendorff, R. Memming, *J. Phys. Chem. B* 101 (1997) 4265–4275.
- [48] W.J. Wang, J.C. Yu, P.K. Wong, R.J. Tayade, *Photocatalytic Materials & Surface for Environmental Cleanup-II*, Trans Tech Publications, Switzerland, 2013, pp. 63–89.
- [49] S.B. Zhu, T.G. Xu, H.B. Fu, J.C. Zhao, Y.F. Zhu, *Environ. Sci. Technol.* 41 (2007) 6234–6239.
- [50] Z.Q. He, Y.Q. Shi, C. Gao, L.N. Wen, J.M. Chen, S. Song, *J. Phys. Chem. C* 118 (2014) 389–398.
- [51] Y. Xu, S.C. Xu, S. Wang, Y.X. Zhang, G.H. Li, *Dalton Trans.* 43 (2014) 479–485.